AGU PUBLICATIONS

Geophysical Research Letters

RESEARCH LETTER
10.1002/2016GL068408

Key Points:
- New TAG sediment core used to examine hydrothermal response to sea level change
- Hydrothermal Fe and Cu deposition peak during Last Glacial Maximum and decline during deglaciation
- Global hydrothermal Fe flux and subsequent carbon export may vary across glacial cycles

Supporting Information:
- Text S1 and Figures S1–S4
- Table S1
- Table S2
- Table S3
- Table S4
- Table S5

Correspondence to:
J. L. Middleton,
jmiddlet@fas.harvard.edu

Citation:
Middleton, J. L., C. H. Langmuir, S. Mukhopadhyay, J. F. McManus, and J. X. Mitrovica (2016), Hydrothermal iron flux variability following rapid sea level changes, *Geophys. Res. Lett.*, *43*, doi:10.1002/2016GL068408.

Received 20 NOV 2015
Accepted 9 APR 2016
Accepted article online 13 APR 2016

Hydrothermal iron flux variability following rapid sea level changes

Jennifer L. Middleton[1,2], Charles H. Langmuir[1], Sujoy Mukhopadhyay[2], Jerry F. McManus[3,4], and Jerry X. Mitrovica[1]

[1]Department of Earth and Planetary Sciences, Harvard University, Cambridge, Massachusetts, USA, [2]Department of Earth and Planetary Sciences, University of California, Davis, California, USA, [3]Lamont-Doherty Earth Observatory, Palisades, New York, USA, [4]Department of Earth and Environmental Sciences, Columbia University, New York, New York, USA

Abstract Sea level changes associated with Pleistocene glacial cycles have been hypothesized to modulate melt production and hydrothermal activity at ocean ridges, yet little is known about fluctuations in hydrothermal circulation on time scales longer than a few millennia. We present a high-resolution record of hydrothermal activity over the past 50 ka using elemental flux data from a new sediment core from the Mir zone of the TAG hydrothermal field at 26°N on the Mid-Atlantic Ridge. Mir sediments reveal sixfold to eightfold increases in hydrothermal iron and copper deposition during the Last Glacial Maximum, followed by a rapid decline during the sea level rise associated with deglaciation. Our results, along with previous observations from Pacific and Atlantic spreading centers, indicate that rapid sea level changes influence hydrothermal output on mid-ocean ridges. Thus, climate variability may discretize volcanic processing of the solid Earth on millennial time scales and subsequently stimulate variability in biogeochemical interactions with volcanic systems.

1. Introduction

Recent studies propose that pressure changes due to rapid sea level fluctuations associated with Pleistocene glacial cycles may influence submarine volcanic activity, with falling sea level driving increased melt production [*Huybers and Langmuir*, 2009; *Lund and Asimow*, 2011; *Crowley et al*., 2015]. Glacially driven changes in submarine volcanism might generate variations in crustal thickness associated with abyssal hills [*Huybers and Langmuir*, 2009; *Crowley et al*., 2015; *Tolstoy*, 2015] and may induce global variations in both magmatic CO_2 emissions [*Burley and Katz*, 2015] and hydrothermal element fluxes across glacial-interglacial cycles [*Lund and Asimow*, 2011]. Hydrothermal circulation provides a deep source of dissolved Fe and other metals to the global oceans [*Conway and John*, 2014; *Fitzsimmons et al*., 2014; *Resing et al*., 2015]. If rapid sea level changes modulate hydrothermal activity, then the global hydrothermal iron flux to nutrient-limited surface waters, and resulting carbon export [e.g., *Tagliabue et al*., 2010], may vary substantially across glacial cycles.

Near-vent sediment cores containing hydrothermal plume precipitates provide continuous, spatially integrated, and datable records to examine the long-term behavior of hydrothermal vent systems [e.g., *Frank et al*., 1994; *Cherkashev*, 1995; *Auffret et al*., 1996; *German et al*., 1997; *Cave et al*., 2002]. Few published studies, however, contain the appropriate temporal resolution over a sufficiently long time interval to capture hydrothermal changes across a glacial interval. This work examines a new sediment core from the relict Mir hydrothermal zone neighboring the TAG hydrothermal field at 26°N on the Mid-Atlantic Ridge [e.g., *Rona et al*., 1993] to provide such a record of hydrothermal activity for the last 50 ka. The new high-resolution record of Mir zone hydrothermal activity is then used to examine millennial-scale climatic forcing of hydrothermal venting and its implications for hydrothermal Fe fertilization across the Last Glacial Maximum (LGM).

2. Sampling and Methods

Gravity core KN207-2-GGC3 (26.14°N, 44.80°W; 3433 m water depth; 82 cm core length) was collected proximal to the relict Mir zone in the axial valley of the Mid-Atlantic Ridge, with the aim of investigating temporal variations in hydrothermal activity, during cruise KN207-2 of the R/V *Knorr* in June 2012 (Figure 1). GGC3 sediments are typically carbonaceous oozes, with carbonate content ranging from 70 to 90 wt % (Table S1 in the supporting information). Small basalt fragments ($<$255 μm) are sparsely scattered throughout the core.

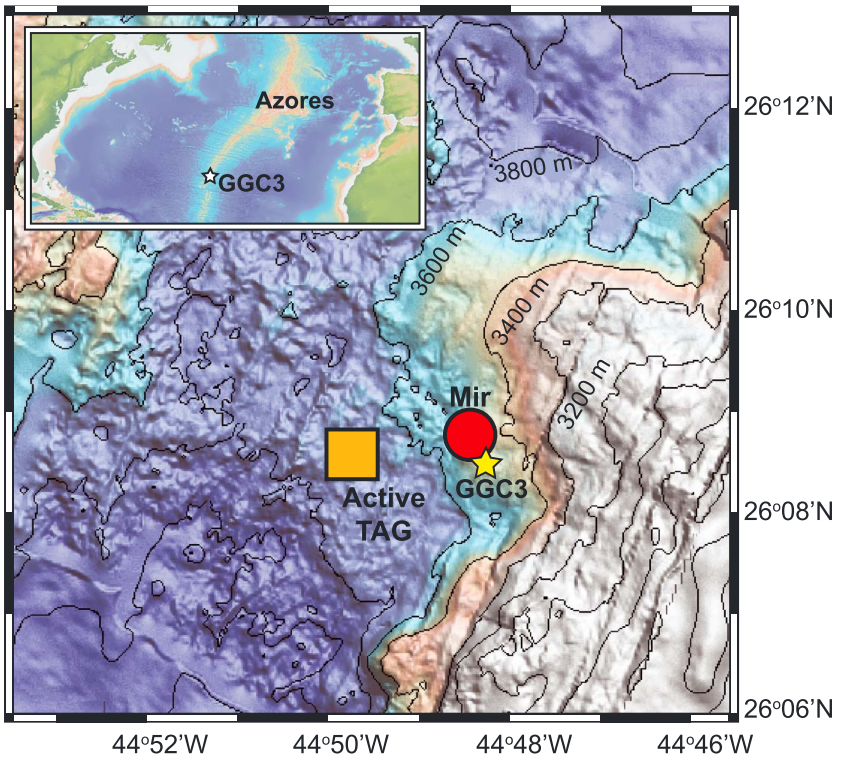

Figure 1. Sediment core location on the Mid-Atlantic Ridge. Gravity core KN207-2-GGC3 (yellow star), the Mir hydrothermal zone (red circle), and the active TAG mound (orange square) within the TAG hydrothermal vent field at 26°N on the Mid-Atlantic Ridge. Contours are shown at 200 m depth intervals. Inset shows the location of GGC3 within the broader context of the northern Mid-Atlantic Ridge.

The full core length was sampled in continuous 1 to 2 cm intervals and reported measurements reflect the average value over the time-depth interval sampled.

Hydrothermal deposition to the Mir zone was constrained using Fe, Cu, Ti, and Th concentrations, obtained using solution nebulized inductively coupled plasma mass spectrometry (ICP-MS; Table S1 in the supporting information) and helium isotope analyses (Tables S2 and S3 in the supporting information). Sediment chronology was determined from benthic foraminiferal oxygen isotope ($\delta^{18}O$) stratigraphy measured in *Cibicidoides wuellerstorfi* (Table S4 in the supporting information), with absolute age control from radiocarbon measurements of the planktonic foraminifer *Globigerinoides ruber* (Table S5 in the supporting information).

2.1. Elemental Flux Determination

Fe, Cu, Ti, and Th concentrations were measured using solution nebulized ICP-MS analyses on a Thermo X series quadrupole at Harvard University (Table S1 in the supporting information) [e.g., *Gale et al.*, 2011]. ICP-MS analyses were performed separately for the carbonate and carbonate-free components of each sample. Initial ICP-MS sample aliquots varied from ~70 to 200 mg in order that the carbonate-free component had a dry mass of ~25 mg. Carbonate components were isolated from bulk sediments using a 24 h leach in 10% acetic acid at 25°C. Some fraction of hydrothermal Fe and Cu may have dissolved during the acetic acid leach and may be detectable within the carbonate leachate composition rather than the carbonate-free sediment composition (Table S1 in the supporting information). To reduce uncertainties associated with this possible fractionation, reported elemental concentrations and fluxes refer to the bulk sediment composition and thus account for both the acetic acid leachate and carbonate-free sediment compositions. Carbonate-free sediments were further digested over several days in a mixture of 0.8 mL of 48% hydrofluoric acid (HF) and 2 mL of 8 N nitric acid (HNO_3) at ~150°C. Once dissolved, the carbonate-free sediments were evaporated at ~100°C and dissolved again with 2.5 mL of 8 N HNO_3, twice, to eliminate residual HF. All acids used in ICP-MS sample preparation were ultrapure grade and double distilled to avoid trace element contamination.

Prior to analysis, the acetic acid leachate and the dissolved carbonate-free sediments were each diluted 1:5000 with an internal standard solution of 0.2 N HNO_3 spiked with Ge (10 ppb), Rh (5 ppb), In (5 ppb), Tm (5 ppb), and Bi (5 ppb). ICP-MS sensitivity to the internal standard elements was used to correct for instrumental drift. Elemental concentrations were calculated from ICP-MS results using calibration curves determined from the standards BCR-2, BHVO-2, DNC-1, W-2, and JB-2 (each digested following the procedure for carbonate-free sediments and analyzed in the same instrumental runs as the sediment samples). Aliquots of the in-house standard K1919 were analyzed between every three samples. The 1σ uncertainties in elemental concentrations were calculated from interrun reproducibility of K1919 and were 0.1 wt %, 0.5 wt %, 4 ppm, and 0.1 ppm for Fe, Ti, Cu, and Th, respectively.

Elemental fluxes were calculated by multiplying concentration values with sediment rain rates derived using extraterrestrial ^{3}He ($^3He_{ET}$) as a constant flux proxy [e.g., *Marcantonio et al*., 2001; *McGee and Mukhopadhyay*, 2013]. The term "rain rate" describes the vertical sediment flux as distinct from the total mass accumulation rate that includes laterally advected material. Marine sediments accumulate $^3He_{ET}$ via the delivery of interplanetary dust particles (IDPs) bearing high $^3He/^4He$ ratios from implanted solar wind. While IDPs dominate the ^{3}He component of deep-sea sediments, terrigenous dust dominates that of ^{4}He [*Patterson et al*., 1999]. The 5 orders of magnitude difference in $^3He/^4He$ ratios between IDPs (~170 R_A, where R_A is the ratio normalized to the atmospheric $^3He/^4He$ ratio of 1.39×10^{-6}) and terrigenous materials (~0.01 R_A) allows for the determination of both $^3He_{ET}$ and terrigenous ^{4}He ($^4He_{terr}$) concentrations in marine sediments under the assumption of two-component mixing (see supporting information) [*McGee and Mukhopadhyay*, 2013].

Sediment concentrations of $^3He_{ET}$ are controlled by both the IDP $^3He_{ET}$ flux from space (f) and the sediment rain rate (Φ) through the relationship $[^3He_{ET}] = fR/\Phi$, where R is the fraction of He retained within the sediments [*McGee and Mukhopadhyay*, 2013]. Retention of $^3He_{ET}$ in ~480 Ma limestone deposits suggests that variations in R over relatively short geologic intervals are negligible [*Patterson et al*., 1998]. Thus, when the IDP $^3He_{ET}$ flux is known, $[^3He_{ET}]$ can be inverted to compute sediment rain rates independent of age-model tie points. Previous work has demonstrated a constant Quaternary IDP $^3He_{ET}$ flux [*Higgins*, 2001; *Marcantonio et al*., 2001; *Winckler and Fischer*, 2006], and a value of $7.7 \pm 1.7 \times 10^{-13}$ cm^3 STP cm^{-2} ka^{-1} [*Higgins*, 2001] was used here.

Helium concentrations and isotope ratios were measured in the <64 μm fraction of initial 1.5 g aliquots of dry bulk sediment. The He aliquots were sieved to provide material for δ^{18}O and radiocarbon measurements and to reduce possible contamination from mid-ocean ridge basalt glass (see supporting information). Sieving does not affect determination of sediment $^3He_{ET}$ because >80%, and possibly >95%, of $^3He_{ET}$-bearing particles reside within the <64 μm sediment fraction [*Mukhopadhyay and Farley*, 2006; *Brook et al*., 2009; *Torfstein*, 2012]. Samples were decarbonated using 10% acetic acid, rinsed 3 times with distilled water, frozen with liquid nitrogen, wrapped in tin foil, and dried for 4 h at 100°C prior to loading into the gas extraction line of the Harvard Noble Gas Laboratory. Sediment helium was extracted under vacuum at 1285°C and measured in a Nu Noblesse mass spectrometer under established protocols [*Mukhopadhyay and Kreycik*, 2008].

Concentrations of $^3He_{ET}$ and $^4He_{terr}$ were calculated assuming a two-component mixture of 170 R_A IDP helium ($(^3He/^4He)_{ET}$) [*Nier and Schlutter*, 1992] and a typical 0.01 R_A terrigenous source ($(^3He/^4He)_{terr}$) [*Farley and Patterson*, 1995] using the following relationship:

$$^3He_{ET} = {}^3He_{msr}\left(\frac{1-\frac{(^3He/^4He)_{terr}}{(^3He/^4He)_{msr}}}{1-\frac{(^3He/^4He)_{terr}}{(^3He/^4He)_{ET}}}\right)$$

where *msr* denotes the measured sample value (Tables S2 and S3 and Figure S1 in the supporting information). The 1σ uncertainties in sediment concentrations of $^3He_{ET}$ and $^4He_{terr}$ were 28% and 1–2%, respectively, and were determined from 108 replicated sample analyses (see supporting information).

2.2. Sediment Chronology

Benthic δ^{18}O measurements were collected on a dual-inlet Thermo Delta V+ mass spectrometer at the Lamont-Doherty Earth Observatory of Columbia University. Whole *C. wuellerstorfi* tests were sonicated in distilled H_2O prior to analysis. Approximately 50 to 90 μg allotments of *C. wuellerstorfi* were dissolved in ~105% phosphoric acid (H_3PO_4) in a Kiel IV device. The resulting CO_2 gas was then purified and analyzed. The NBS-19

international standard was analyzed every ~10 samples. The long-term standard deviation for $\delta^{18}O$ of NBS-19 measured on this instrument is 0.06‰. The average difference in $\delta^{18}O$ between replicated samples was 0.24‰ (Table S4 in the supporting information).

Radiocarbon measurements were conducted at the National Ocean Sciences Accelerator Mass Spectrometry (NOSAMS) Facility at the Woods Hole Oceanographic Institution (Table S5 in the supporting information). Whole *G. ruber* tests were sonicated for 30 s in ethanol, followed by >1 min of sonication in distilled H_2O prior to submission to the NOSAMS facility to reduce sedimentary contamination. NOSAMS radiocarbon sample ages were corrected for a 400 year North Atlantic surface ocean reservoir age [*Bard*, 1988]. The sediment core age model was then calculated between radiocarbon dated depths assuming constant sedimentation rates between tie points. One radiocarbon sample (GGC3: 64–66 cm) yielded an age >35 ka and was not included in age model calculations. Ages for sediment core depths lower than the oldest tie point were estimated using the same constant sedimentation rate as the previous tie point bounded sediment interval. The radiocarbon-derived timing of LGM matches the maximum values of the $\delta^{18}O$ stratigraphy in GGC3.

2.3. Relative Sea Level Curve

The sea level history at the TAG hydrothermal field site was computed across the last glacial cycle using a gravitationally self-consistent theory that accounts for Maxwell viscoelastic adjustment of the solid Earth, time-varying shoreline geometry, and changes in Earth rotation [*Mitrovica and Milne*, 2003; *Kendall et al*., 2005], using a pseudo-spectral algorithm with truncation at spherical harmonic degree and order 256 [*Kendall et al*., 2005]. The predicted sea level history for the TAG hydrothermal field is relatively insensitive to changes in the ice history and Earth model, including the incorporation of lateral variations in lithospheric thickness and mantle viscosity (Figure S4 in the supporting information).

3. Results

Hydrothermal contributions to Mir sediments were identified using Fe and Cu, as both are enriched in near-vent (≤5 km) hydrothermal deposits [*Cave et al*., 2002]. Total sediment Fe and Cu contents, however, can also reflect contributions from terrigenous dust and mid-ocean ridge basalt fragments. The terrigenous component was constrained using $^4He_{terr}$ and Th, both excellent tracers of dust [*Patterson et al*., 1999; *Winckler et al*., 2008]. In addition, Fe/Ti and Cu/Ti ratios were used to distinguish hydrothermal material from Fe and Cu associated with dust and basalt fragment.

The highest Fe and Cu concentrations occur between 30 and 50 cm depth and coincide with the LGM, as indicated by the heaviest $\delta^{18}O$ values (Figure 2). The LGM peak in Fe and Cu requires enhanced hydrothermal deposition because the synchronous Fe and Cu patterns are distinct from the dust proxies, Th and $^4He_{terr}$, which broadly oscillate throughout the core (Figure 2). The background Fe/Ti ratio of 13 to 22 suggests a small, but near-continuous, hydrothermal sediment contribution as the Fe/Ti ratios of dust and basalt are ~11.7 [*Taylor and McLennan*, 1995] and ~8.3 [*Gale et al*., 2013], respectively. The pronounced peak in the Fe/Ti ratio to 71 ± 16 across the LGM (Figure 2e), therefore, requires a significant increase in hydrothermal Fe deposition.

Fe and Cu fluxes confirm an increase in hydrothermal deposition across the LGM (Figure 3). The LGM peak in Fe and Cu concentrations represents a fourfold increase in total Fe flux and a sevenfold increase in total Cu flux between 28 and 15 ka (Figures 3a and 3b). In contrast, the dust fluxes, as constrained by Th and $^4He_{terr}$, remain relatively constant between 28 and 15 ka. The dust fluxes peak, instead, between 15 and 10 ka, when Fe and Cu fluxes are in decline (Figures 3d and 3e). Thus, the elemental flux data indicate that increased Fe and Cu deposition during the LGM must come from enhanced hydrothermal activity and not from enhanced terrigenous input.

Hydrothermal fluxes (X_{HT}) were more precisely distinguished from total Fe and Cu fluxes (X_{total}) following the relationship $X_{HT} = X_{total} - (X/Ti)_{nonHT} \times Ti_{total}$, where $(X/Ti)_{nonHT}$ represents the X/Ti ratio of non-hydrothermal components (dust and basalt; Figures 3a and 3c). $(Cu/Ti)_{nonHT}$ can be estimated using the terrigenous Cu/Ti value (83 ppm/wt %) [*Taylor and McLennan*, 1995] because terrigenous Cu/Ti and mid-ocean ridge basalt Cu/Ti (80 ppm/wt %) [*Gale et al*., 2013] are vastly lower than the highest measured hydrothermal sediment values in GGC3 (>30,000 ppm/wt %). $(Fe/Ti)_{nonHT}$ can similarly be approximated using the terrigenous Fe/Ti value of ~11.7 [*Taylor and McLennan*, 1995]. Dust and basalt corrections to the elemental fluxes are

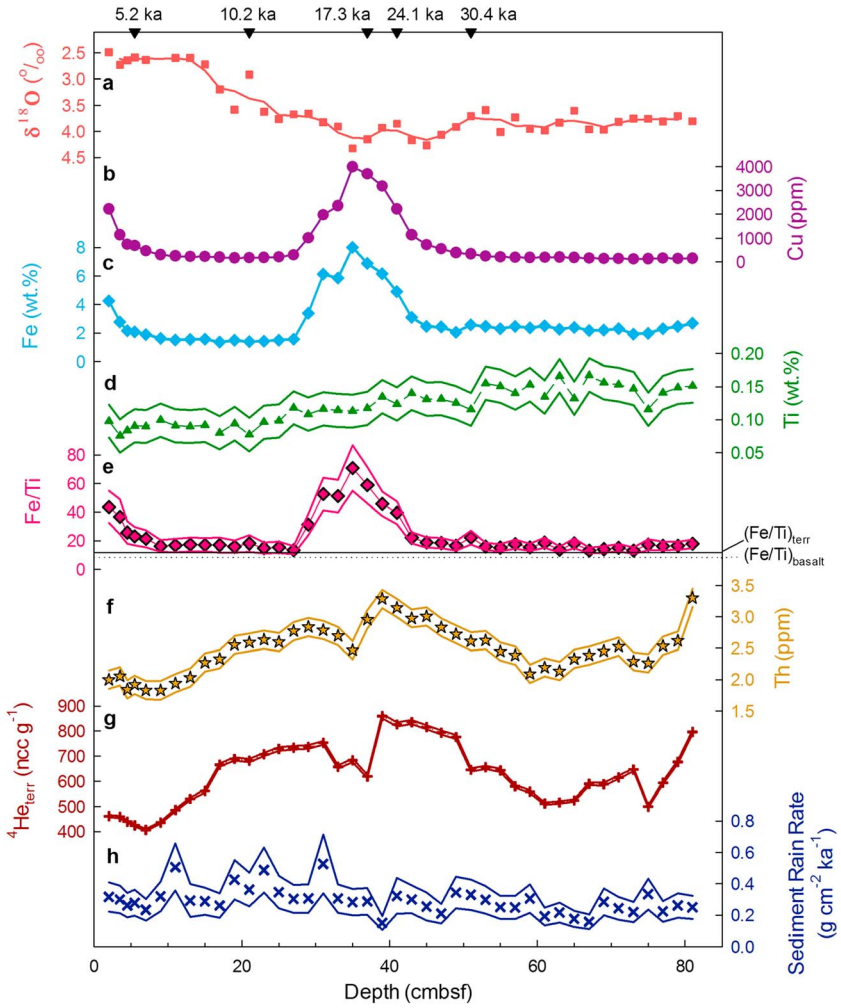

Figure 2. Sediment composition as a function of depth. (a) Benthic $\delta^{18}O$ values from *C. wuellerstorfi* for each depth (squares), along with the $\delta^{18}O$ three-point running mean (solid line), and depths with planktonic *G. ruber* radiocarbon dates (black triangles). Bulk sediment concentrations of (b) Cu, (c) Fe, (d) Ti, (e) the Fe/Ti ratio, (f) bulk sediment Th, and (g) terrigenous ^4He ($^4He_{terr}$) for each depth (points) within 1σ uncertainty envelope (solid lines). (h) Extraterrestrial ^3He ($^3He_{ET}$)-derived sediment rain rates for each depth (points) within a 1σ uncertainty envelope (solid lines). The Fe/Ti values for terrigenous material (11.7, solid black line) and mid-ocean ridge basalt (8.3, dashed black line) are highlighted in Figure 2e [*Taylor and McLennan*, 1995; *Gale et al.*, 2013].

minor, as hydrothermal Fe and Cu compose >80% and >90% of total Fe and Cu fluxes, respectively, during the LGM hydrothermal peak (Figure S2 in the supporting information). With the non-hydrothermal background removed, corrected fluxes indicate a sixfold to eightfold increase in hydrothermal Fe and Cu deposition between 28 and 15 ka.

4. Discussion

We interpret observed variations in hydrothermal deposition to reflect changes in hydrothermal output from the Mir vent field. Discrete uranium series dates of Mir zone sulfides demonstrate active intervals of Mir hydrothermal venting at 0.7–3 ka and at 18–20 ka [*Lalou et al.*, 1995] that align with both periods of enhanced hydrothermal deposition observed in GGC3 sediments.

Conceivably, repeated debris flow deposition of weathered sulfides from the Mir vent field, rather than mineral precipitation from an overlying hydrothermal plume, could generate the hydrothermal signal observed in GGC3. However, there is no sedimentological evidence for debris flow deposition within the core and neither the radiocarbon data, nor the benthic $\delta^{18}O$ stratigraphy, nor the $^3He_{ET}$-derived mass

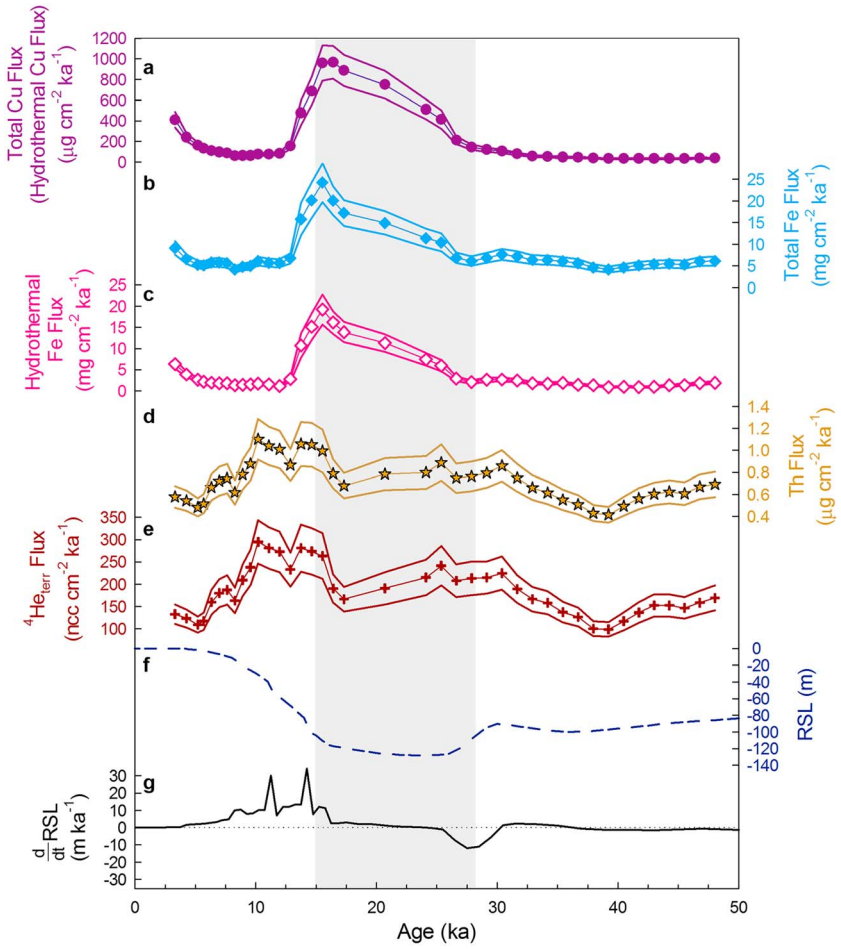

Figure 3. Comparison of elemental flux data and sea level history. The three-point running mean elemental fluxes (points) and 1σ uncertainty envelopes for (a) total Cu and hydrothermal Cu, which completely overlap on the figure scale, (b) total Fe, (c) hydrothermal Fe, (d) dust proxies Th, and (e) $^4He_{terr}$. (f) Relative sea level curve (RSL) and (g) rate of sea level change ($^d/_{dt}$ RSL) computed for TAG hydrothermal field at 26°N on the Mid-Atlantic Ridge. The gray bar highlights the concurrent changes in the rate of sea level fall and rise with the respective rise and fall of hydrothermal fluxes across the LGM (28–15 ka).

accumulation rates of GGC3 sediments show signs of significant disruption in sediment chronology or accumulation (Figure 2). Varying bottom currents could change the directionality of the Mir hydrothermal plume and potentially provide an alternate explanation for variable hydrothermal deposition to the core. However, comparison of the down-core Fe contents of GGC3 and of four neighboring Mir zone sediment cores [*Cherkashev*, 1995] reveals a spatially consistent pattern of hydrothermal deposition on all sides of the Mir hydrothermal system (Figure S3 in the supporting information). Although sampling resolution and sedimentation rates vary slightly among the suite of Mir cores, the four *Cherkashev* [1995] cores contain both a core top Fe peak and a 30–50 cm depth Fe peak, as observed in GGC3. If the variations in hydrothermal deposition to GGC3 sediments were driven by changes in debris flow activity, or by plume directionality alone, then there should not be a reproducible Fe pattern in multiple directions surrounding the Mir zone. Ultimately, net changes in Mir hydrothermal output provide the best explanation for the hydrothermal sedimentation fluctuations observed in GGC3.

Absolute age control allows for comparison of the Mir zone hydrothermal record with a relative sea level (RSL) curve calculated for the TAG hydrothermal field across the last glacial cycle (Figures 3f and 3g). The RSL time series presented in Figure 3 was computed using the ICE-5G (version 1.2) ice model and the VM2 mantle viscosity profile [*Peltier*, 2004] (Figure S4 in the supporting information).

The amplitude and timing of Mir zone hydrothermal variability suggests a relationship between rapid sea level change and hydrothermal activity. Fe and Cu fluxes reveal increased hydrothermal deposition between

28 and 15 ka and again between 7 and 2 ka. The smaller peak in hydrothermal activity between 7 and 2 ka does not coincide with rapid sea level changes and may be driven by local tectonic or magmatic factors [*Lalou et al*., 1995]. However, the largest hydrothermal signal observed in GGC3 (28 to 15 ka) clearly coincides with the sea level minimum associated with LGM (Figure 3).

The data suggest a relatively swift hydrothermal response following a rapid sea level change. The onset of increased hydrothermal deposition at 28 ka coincides with the fastest rate of sea level fall, and thus the fastest rate of sea level pressure decrease, during the last 50 ka. The end of the enhanced hydrothermal period, marked by the maximum hydrothermal sediment flux at 15 ka, occurs at the onset of rapid sea level rise associated with global-scale deglaciation. A major reduction in hydrothermal activity follows and coincides with Meltwater Pulse 1A (MWP-1A) at ~14.5 ka, during which global mean sea level rose ~15 m in less than 340 years [*Deschamps et al*., 2012]. Both the increase in hydrothermal activity associated with rapid sea level fall and the decrease associated with rapid sea level rise are consistent with the hypothesis that hydrothermal circulation responds to sea level change.

Enhanced hydrothermal activity across the LGM and across Marine Isotope Stage 4 has also been observed in sediment cores from the Galapagos Microplate [*Frank et al*., 1994] and from 38°N on the Mid-Atlantic Ridge [*Auffret et al*., 1996], suggesting a global ridge response to sea level change [*Lund and Asimow*, 2011]. Further evidence for a global ridge response to sea level change comes from recent analyses of sediment cores from the southern East Pacific Rise that reveal peaks in hydrothermal deposition following LGM and the previous glaciation [*Lund et al*., 2016]. At the Mir zone, the onset of the LGM-associated increase in hydrothermal activity occurs at ~27 ka, near concurrently with the fastest rate of sea level fall. In contrast, the onset of the LGM-associated increase in hydrothermal activity at 6°S on the southern East Pacific Rise appears to lag the sea level signal by up to 5 ka. Such variations in timing merit further investigation into the diverse manifestation of hydrothermal responses to sea level change. However, it is notable that the peak hydrothermal fluxes at both locations occur at ~15 ka, just before the onset of major deglaciation.

While climatic and volcanic interactions are known to occur on multimillion year time scales, as with the deep carbon cycle, a global LGM hydrothermal peak suggests volcanic sensitivity to millennial-scale climate variability. Furthermore, climate modulation of the chemical cycling and redox exchange at submarine volcanic settings could stimulate additional variability in biogeochemical interactions with the solid Earth. The twofold to fourfold increases in hydrothermal deposition from ~35 ka to the LGM observed in the previous studies [*Frank et al*., 1994; *Auffret et al*., 1996; *Lund and Asimow*, 2011; *Lund et al*., 2016] are lower than the sixfold to eightfold Mir increase, yet even a conservative threefold LGM spike in global hydrothermal output would be comparable in Fe flux magnitude to the twofold to fourfold increase in global dust flux during the last glacial period [*Mahowald et al*., 2006; *Winckler et al*., 2008].

Globally synchronous hydrothermal variation could have dramatic effects on hydrothermal Fe availability, biological carbon export, and the drawdown of atmospheric CO_2 in the Southern Ocean and other Fe-limited waters. Organic ligand complexation permits transport of dissolved hydrothermal Fe both high into the water column and far (>4000 km) from its vent source [*Bennett et al*., 2008; *Toner et al*., 2009; *Conway and John*, 2014; *Fitzsimmons et al*., 2014; *Resing et al*., 2015]. Recent biogeochemical models including such transport suggest that the modern hydrothermal flux yields 4 Gmol yr^{-1} of dissolved hydrothermal Fe and may stimulate ~15–30% of carbon export in parts of the Southern Ocean [*Tagliabue et al*., 2010; *Saito et al*., 2013; *Resing et al*., 2015].

If the modern hydrothermal flux represents the global background at 30 ka, then a threefold increase in hydrothermal Fe output may have delivered significantly more dissolved Fe to the global oceans and could have enhanced carbon export in otherwise Fe-limited surface waters. Full quantification of the resulting dissolved Fe flux is beyond the scope of this work, as Fe stabilizing ligands may saturate with increased Fe flux or, if they are produced by hydrothermal ecosystems, may vary in concentration with increased hydrothermal activity [*Bennett et al*., 2008; *Toner et al*., 2009]. Assuming that a constant fraction of hydrothermal Fe is stabilized in the dissolved phase, however, a threefold increase in the global hydrothermal output of ~4 Gmol yr^{-1} [*Resing et al*., 2015] would yield a dissolved hydrothermal Fe flux of ~12 Gmol yr^{-1}. Wind-blown dust provides the largest Fe source to the open ocean, and assuming a terrigenous Fe solubility of 5%, the modern dust flux to the ocean yields a comparable value of ~14 Gmol yr^{-1} of dissolved Fe [*Jickells et al*., 2005]. Although enhanced carbon export may not scale linearly with increased hydrothermal flux [e.g., *Tagliabue et al*., 2010],

a threefold increase in hydrothermal activity during the LGM suggests that hydrothermal Fe does not buffer the ocean from glacial-interglacial variations in dust deposition as previously proposed, but may instead vary to a similar degree, and should therefore be considered in future calculations and modeling efforts.

5. Conclusions

We examine hydrothermal flux variations over the past 50 ka in a Mir zone sediment core from the TAG vent field on the Mid-Atlantic Ridge to test the hypothesis that Pleistocene sea level fluctuations modulate submarine hydrothermal activity. Hydrothermal fluxes were constrained using $^{3}He_{ET}$-derived sediment rain rates and measurements of Fe, Cu, Th, $^{4}He_{terr}$, and Ti. The Mir sediments record a sixfold to eightfold increase in hydrothermal Fe and Cu deposition between 28 and 15 ka, coinciding with the LGM. The onset of the Mir hydrothermal peak occurs at ~28 ka and coincides with the fastest rate of sea level fall entering LGM. Hydrothermal deposition quickly returns to baseline after 15 ka, during the main phase of global deglaciation that includes the MWP-1A event.

Our results, along with previous sediment analyses from the Galapagos Microplate, from the southern East Pacific Rise, and from 38°N on the Mid-Atlantic Ridge, indicate that hydrothermal systems respond to rapid sea level changes and suggest that the global hydrothermal Fe flux may have been significantly higher during the LGM than observed today. Increased hydrothermal Fe output during the LGM could lead to enhanced Fe fertilization, carbon export, and the drawdown of atmospheric CO_2 in the Southern Ocean and other Fe-limited waters. Ultimately, the magnitude of global hydrothermal emissions and resulting effects on marine biogeochemical cycles may vary in pace with Pleistocene glacial variability.

Acknowledgments

All data in this paper are available in the supporting tables and references. We thank the captain, crew, and science party of the R/V *Knorr* on cruise KN2072-2 for their assistance at sea; W. Huang, B. Linsley, and Z. Chen for technical assistance with oxygen isotope and ICP-MS analyses; E. Roosen and A. Saxby for assistance in core sampling and sample preparation; and P. Huybers and K. Costa for helpful discussions. We also thank two anonymous reviewers for their useful comments. We acknowledge financial support from the National Science Foundation grant AGS-1338832 and the NOSAMS National Science Foundation cooperative agreement OCE-1239667.

References

Auffret, G. A., et al. (1996), Record of hydrothermal activity in sediments from the Mid-Atlantic Ridge south of the Azores, *C. R. Acad. Sci.*, *323*(7), 583–590.

Bard, E. (1988), Correction of accelerator mass spectrometry ^{14}C ages measured in planktonic foraminifera: Paleoceanographic implications, *Paleoceanography*, *3*, 635–645, doi:10.1029/PA003i006p00635.

Bennett, S. A., E. P. Achterberg, D. P. Connelly, P. J. Statham, G. R. Fones, and C. R. German (2008), The distribution and stabilisation of dissolved Fe in deep-sea hydrothermal plumes, *Earth Planet. Sci. Lett.*, *270*(3), 157–167.

Brook, E. J., M. D. Kurz, and J. Curtice (2009), Flux and size fractionation of ^{3}He in interplanetary dust from Antarctic ice core samples, *Earth Planet. Sci. Lett.*, *286*(3-4), 565–569.

Burley, J., and R. F. Katz (2015), Variations in mid-ocean ridge CO_2 emissions driven by glacial cycles, *Earth Planet. Sci. Lett.*, *426*, 246–258.

Cave, R. R., C. R. German, J. Thomson, and R. W. Nesbitt (2002), Fluxes to sediments underlying the rainbow hydrothermal plume at 36°14′N on the Mid-Atlantic Ridge, *Geochim. Cosmochim. Acta*, *66*(11), 1905–1923.

Cherkashev, G. (1995), Hydrothermal input into sediments of the Mid-Atlantic Ridge, *Geol. Soc. London Spec. Publ.*, *87*(1), 223–229.

Conway, T. M., and S. G. John (2014), Quantification of dissolved iron sources to the North Atlantic Ocean, *Nature*, *511*(7508), 212–215.

Crowley, J. W., R. F. Katz, P. Huybers, C. H. Langmuir, and S.-H. Park (2015), Glacial cycles drive variations in the production of oceanic crust, *Science*, *347*(6227), 1237–1240.

Deschamps, P., N. Durand, E. Bard, B. Hamelin, G. Camoin, A. L. Thomas, G. M. Henderson, J. Okuno, and Y. Yokoyama (2012), Ice-sheet collapse and sea-level rise at the Bolling warming 14,600 years ago, *Nature*, *483*(7391), 559–564.

Farley, K. A., and D. B. Patterson (1995), A 100-kyr periodicity in the flux of extraterrestrial ^{3}He to the sea floor, *Nature*, *378*(6557), 600–603.

Fitzsimmons, J. N., E. A. Boyle, and W. J. Jenkins (2014), Distal transport of dissolved hydrothermal iron in the deep South Pacific Ocean, *Proc. Natl. Acad. Sci. U.S.A.*, *111*(47), 16,654–16,661.

Frank, M., J.-D. Eckhardt, A. Eisenhauer, P. W. Kubik, B. Dittrich-Hannen, M. Segl, and A. Mangini (1994), Beryllium 10, thorium 230, and protactinium 231 in Galapagos microplate sediments: Implications of hydrothermal activity and paleoproductivity changes during the last 100,000 years, *Paleoceanography*, *9*, 559–578, doi:10.1029/94PA01132.

Gale, A., S. Escrig, E. J. Gier, C. H. Langmuir, and S. L. Goldstein (2011), Enriched basalts at segment centers: The Lucky Strike (37°17′N) and Menez Gwen (37°50′N) segments of the Mid-Atlantic Ridge, *Geochem. Geophys. Geosyst.*, *12*, Q06016, doi:10.1029/2010GC003446.

Gale, A., C. A. Dalton, C. H. Langmuir, Y. Su, and J.-G. Schilling (2013), The mean composition of ocean ridge basalts, *Geochem. Geophys. Geosyst.*, *14*, 489–518, doi:10.1029/2012GC004334.

German, C. R., et al. (1997), Hydrothermal scavenging on the Juan de Fuca Ridge: Th-230(xs), Be-10, and REEs in ridge-flank sediments, *Geochim. Cosmochim. Acta*, *61*(19), 4067–4078.

Higgins, S. (2001), *Extraterrestrial Tracer in the Sea: Evaluation and Application of ^{3}He in Interplanetary Dust Particles as a "Constant Flux" Tracer in Marine Sediments*, Columbia Univ., New York.

Huybers, P., and C. Langmuir (2009), Feedback between deglaciation, volcanism, and atmospheric CO_2, *Earth Planet. Sci. Lett.*, *286*(3), 479–491.

Jickells, T., Z. An, K. K. Andersen, A. Baker, G. Bergametti, N. Brooks, J. Cao, P. Boyd, R. Duce, and K. Hunter (2005), Global iron connections between desert dust, ocean biogeochemistry, and climate, *Science*, *308*(5718), 67–71.

Kendall, R. A., J. X. Mitrovica, and G. A. Milne (2005), On post-glacial sea level—II. Numerical formulation and comparative results on spherically symmetric models, *Geophys. J. Int.*, *161*(3), 679–706.

Lalou, C., J. L. Reyss, E. Brichet, P. A. Rona, and G. Thompson (1995), Hydrothermal activity on a 10^{5}-year scale at a slow-spreading ridge, TAG hydrothermal field, Mid-Atlantic Ridge 26°N, *J. Geophys. Res.*, *100*, 17,855–17,862, doi:10.1029/95JB01858.

Lund, D. C., and P. D. Asimow (2011), Does sea level influence mid-ocean ridge magmatism on Milankovitch timescales?, *Geochem. Geophys. Geosyst.*, *12*, Q12009, doi:10.1029/2011GC003693.

Lund, D. C., P. D. Asimow, K. A. Farley, T. O. Rooney, E. Seeley, E. W. Jackson, and Z. M. Durham (2016), Enhanced East Pacific Rise hydrothermal activity during the last two glacial terminations, *Science*, *351*(6273), 478–482.

Mahowald, N. M., D. R. Muhs, S. Levis, P. J. Rasch, M. Yoshioka, C. S. Zender, and C. Luo (2006), Change in atmospheric mineral aerosols in response to climate: Last glacial period, preindustrial, modern, and doubled carbon dioxide climates, *J. Geophys. Res.*, *111*, D10202, doi:10.1029/2005JD006653.

Marcantonio, F., R. F. Anderson, S. Higgins, M. Stute, P. Schlosser, and P. Kubik (2001), Sediment focusing in the central equatorial Pacific Ocean, *Paleoceanography*, *16*, 260–267, doi:10.1029/2000PA000540.

McGee, D., and S. Mukhopadhyay (2013), Extraterrestrial He in sediments: From recorder of asteroid collisions to timekeeper of global environmental changes, in *The Noble Gases as Geochemical Tracers*, edited P. Burnard, pp. 155–176, Springer, Hiedelberg, Germany.

Mitrovica, J. X., and G. A. Milne (2003), On post-glacial sea level: I. General theory, *Geophys. J. Int.*, *154*(2), 253–267.

Mukhopadhyay, S., and K. Farley (2006), New insights into the carrier phase(s) of extraterrestrial ^{3}He in geologically old sediments, *Geochim. Cosmochim. Acta*, *70*(19), 5061–5073.

Mukhopadhyay, S., and P. Kreycik (2008), Dust generation and drought patterns in Africa from helium-4 in a modern Cape Verde coral, *Geophys. Res. Lett.*, *35*, L20820, doi:10.1029/2008GL035722.

Nier, A., and D. Schlutter (1992), Extraction of helium from individual interplanetary dust particles by step-heating, *Meteoritics*, *27*(2), 166–173.

Patterson, D., K. Farley, and B. Schmitz (1998), Preservation of extraterrestrial ^{3}He in 480-Ma-old marine limestones, *Earth Planet. Sci. Lett.*, *163*(1), 315–325.

Patterson, D., K. Farley, and M. Norman (1999), ^{4}He as a tracer of continental dust: A 1.9 million year record of aeolian flux to the west equatorial Pacific Ocean, *Geochim. Cosmochim. Acta*, *63*(5), 615–625.

Peltier, W. (2004), Global glacial isostasy and the surface of the ice-age Earth: The ICE-5G (VM2) model and GRACE, *Annu. Rev. Earth Planet. Sci.*, *32*, 111–149.

Resing, J. A., P. N. Sedwick, C. R. German, W. J. Jenkins, J. W. Moffett, B. M. Sohst, and A. Tagliabue (2015), Basin-scale transport of hydrothermal dissolved metals across the South Pacific Ocean, *Nature*, *523*(7559), 200–203.

Rona, P. A., Y. A. Bogdanov, E. G. Gurvich, B. A. Rimski-Korsakov, A. M. Sagalevitch, M. D. Hannington, and G. Thompson (1993), Relict hydrothermal zones in the TAG hydrothermal field, Mid-Atlantic Ridge 26°N, 45°W, *J. Geophys. Res.*, *98*, 9715–9730, doi:10.1029/93JB00552.

Saito, M. A., A. E. Noble, A. Tagliabue, T. J. Goepfert, C. H. Lamborg, and W. J. Jenkins (2013), Slow-spreading submarine ridges in the South Atlantic as a significant oceanic iron source, *Nat. Geosci.*, *6*(9), 775–779.

Tagliabue, A., L. Bopp, J.-C. Dutay, A. R. Bowie, F. Chever, P. Jean-Baptiste, E. Bucciarelli, D. Lannuzel, T. Remenyi, and G. Sarthou (2010), Hydrothermal contribution to the oceanic dissolved iron inventory, *Nat. Geosci.*, *3*(4), 252–256.

Taylor, S. R., and S. M. McLennan (1995), The geochemical evolution of the continental crust, *Rev. Geophys.*, *33*, 241–265, doi:10.1029/95RG00262.

Tolstoy, M. (2015), Mid-ocean ridge eruptions as a climate valve, *Geophys. Res. Lett.*, *42*, 1346–1351, doi:10.1002/2014GL063015.

Toner, B. M., S. C. Fakra, S. J. Manganini, C. M. Santelli, M. A. Marcus, J. W. Moffett, O. Rouxel, C. R. German, and K. J. Edwards (2009), Preservation of iron (II) by carbon-rich matrices in a hydrothermal plume, *Nat. Geosci.*, *2*(3), 197–201.

Torfstein, A. (2012), Size fractionation, reproducibility and provenance of helium isotopes in north-equatorial Pacific pelagic clays, *Earth Planet. Sci. Lett.*, *339–340*, 151–163.

Winckler, G., and H. Fischer (2006), 30,000 years of cosmic dust in Antarctic ice, *Science*, *313*(5786), 491–491.

Winckler, G., R. F. Anderson, M. Q. Fleisher, D. McGee, and N. Mahowald (2008), Covariant glacial-interglacial dust fluxes in the equatorial Pacific and Antarctica, *Science*, *320*(5872), 93–96.